Constraining Properties of Dark Matter particles Using Astrophysical Data

Iakubovskyi, D.

Cover Page

The handle http://hdl.handle.net/1887/20523 holds various files of this Leiden University dissertation.

Author: Iakubovskyi, Dmytro
Title: Constraining properties of dark matter particles using astrophysical data
Issue Date: 2013-02-13

Chapter 8

Appendixes

8.1 Abbreviations used in this thesis

Below, we collect the full list of abbreviations, used throughout this thesis.

ΛCDM — standard cosmological model

νMSM — Neutrino Minimal Standard Model

ACIS — Advanced Advanced CCD Imaging Spectrometer on-board *Chandra*

ARF — ancillary response function (effective area)

BBN — Big Bang Nucleosynthesis

BOSS — Baryon Oscillation Spectroscopic Survey, a part of SDSS-III

BURK — Burkert density distribution

CCD — charge coupled device

CDM — cold dark matter

Chandra — Chandra X-ray observatory

CMB — cosmic microwave background radiation

CWDM — cold plus warm dark matter

DM — dark matter

dSph — dwarf spheroidal galaxy

EPIC — European Photon Imaging Camera on-board *XMM-Newton*

FoV — field-of-view

FSH — free-streaming horizon

FWHM — full width at half-maximum

HDM — hot dark matter

HEASARC — High-Energy Astrophysics Science Archive Research Center

IS2 — modified pseudo-isothermal density distribution

ISO — pseudo-isothermal density distribution

KiDS — Kilo-Degree Survey

LHC — Large Hadron Collider

LMC — Large Magellanic Cloud

LSS — Large Scale Structure of the Universe

LSST — Large Synoptic Survey Telescope

M31 — Andromeda galaxy

MOS — Metal Oxide Semiconductor camera. Two EPIC cameras (MOS1 and MOS2) on board of *XMM-Newton*

MW — Milky Way galaxy

NFW — Navarro-Frenk-White density distribution

NRP — production of sterile neutrinos through non-resonant oscillations of active neutrinos

PN — p-n (positive-negative) transition. One of the EPIC cameras on board of *XMM-Newton*

RMF – redistribution matrix file (energy resolution)

RP — production of sterile neutrinos through resonant oscillations of active neutrinos

SDSS — Sloan Digital Sky Survey

SMC — Small Magellanic Cloud

TG — Tremaine-Gunn

VLT — Very Large Telescope of European Southern Observatory

WDM — warm dark matter

WFIRST — Wide-Field Infrared Survey Telescope

WIMP — weakly interacting massive particle

WMAP — Wilkinson Microwave Anisotropy Probe

XIS – X-ray Imaging Spectrometer on-board *Suzaku*

XMM-Newton SAS — *XMM-Newton* Science Analysis Software

XMM — *XMM-Newton*, X-ray Multi-Mirror X-ray mission

XRB – cosmic X-ray background

XSPEC — X-Ray Spectral Fitting Package

8.2 Appendixes for Chapter 2

8.2.1 Entropy for different distributions

In this Appendix we will calculate the entropy for several phase-space distributions, including those of (2.4), (2.20), (2.5), and explore its relation with the quantity Q, defined in (2.7).

The entropy of an ideal Fermi gas is given by the expression [420]

$$S = -\int d^3p d^3r f(r,p) \log\left(\frac{(2\pi\hbar)^3 f(r,p)}{g}\right) + \tag{8.1}$$
$$+ \left(\frac{g}{(2\pi\hbar)^3} - f(r,p)\right) \log\left(1 - \frac{(2\pi\hbar)^3 f(r,p)}{g}\right).$$

If the distribution function $f(r,p) \ll \frac{g}{(2\pi\hbar)^3}$, we obtain the expression for the entropy of a non-degenerate ideal gas:

$$S = -\int d^3p d^3r f(r,p) \left[\log\left(\frac{(2\pi\hbar)^3 f(r,p)}{g}\right) - 1\right]. \tag{8.2}$$

8.2.1.1 Ideal Boltzmann gas

We start with the case of ideal Boltzmann gas:

$$f(r,p) = f_0 e^{-\frac{p^2}{2mT}}. \tag{8.3}$$

Substituting it into Eq. (8.2), we arrive to the well-known expression (c.f. e.g. Sec. 42 of [420]):

$$\frac{S}{N} = \frac{5}{2} + \log\left(\frac{gV}{N} \frac{(mT)^{3/2}}{(2\pi\hbar^2)^{3/2}}\right), \tag{8.4}$$

where V is the volume of the system, N is a number of particles. Expressing S/N as a function of $\bar{\rho}$ and $\langle v^2 \rangle$, we finally obtain relation between the entropy and Q in the form (2.10)

$$\frac{S}{N} = \log C_B - \log\frac{Q\hbar^3}{m^4}, \ C_B = g\frac{e^{5/2}}{(6\pi)^{3/2}} \approx g \times 0.1489\ldots \tag{8.5}$$

8.2.1.2 Isothermal phase-space density distrubution

Next, we consider the case when the phase-space density distribution can be approximated by (pseudo)-isothermal sphere (c.f. (2.5)):

$$f_{iso}(r,p) = \frac{9\sigma^2}{4\pi G_N (2\pi m^2 \sigma^2)^{3/2}(r^2 + r_c^2)} e^{-\frac{p^2}{2m^2\sigma^2}}. \tag{8.6}$$

The number of particles in such a system, as well as the total entropy, diverges for large r, however the entropy per particles grows logarithmically at large r and therefore the exact value of cut-off is not important.

Truncating the expression for the entropy at some r_{max} and taking $r_{max} \gg r_c$, we obtain

$$\frac{S}{N} = -\log \frac{Q\hbar^3}{m^4} + \log C_{iso}, \quad C_{iso} = \frac{g \exp(1/2)}{\sqrt{3}(2\pi)^{3/2}} \approx g \times 0.0604\ldots \quad (8.7)$$

8.2.1.3 Non-resonantly produced sterile neutrinos

Next, we analyze the case of primordial momentum distribution, which has the form of (rescaled) relativistic Fermi-Dirac.

$$f(p) = \frac{g}{(2\pi\hbar)^3} \frac{F}{e^{\epsilon(p)/T} + 1}, \quad \epsilon(p) = p . \quad (8.8)$$

For now we keep both F and T to be arbitrary. The distribution in the form (8.8) accounts for both (2.4) and (2.20) cases. The entropy of N particles with distribution (8.8) is given by the expression (8.1), which reduces to

$$S = \frac{gVT^3}{2\pi^2\hbar^3} I(F), \quad (8.9)$$

where function $I(F)$ is given by

$$I(F) \equiv -\int_0^\infty dz z^2 \left[\frac{F}{e^z + 1} \log\left(\frac{F}{e^z + 1}\right) + \left(1 - \frac{F}{e^z + 1}\right) \log\left(1 - \frac{F}{e^z + 1}\right) \right] . \quad (8.10)$$

The integral (8.10) can be computed numerically. At $F \ll 1$ the expression (8.10) can be approximated by

$$I(F) \approx \frac{3}{2}\zeta(3)(F - F \log F) + F \int_0^\infty \frac{dz z^2}{e^z + 1} \log(e^z + 1). \quad (8.11)$$

The specific entropy S/N equals to

$$\frac{S}{N} = \frac{gm^4 I(F)}{2\pi^2\hbar^3} \left(\frac{\zeta(3)}{15\zeta(5)}\right)^{3/2} \frac{\langle v^2 \rangle^{3/2}}{\bar{\rho}} = \frac{g\, I(F)}{2\pi^2} \left(\frac{\zeta(3)}{15\zeta(5)}\right)^{3/2} \frac{m^4}{Q\hbar^3} . \quad (8.12)$$

Therefore, we see that for the distributions of the form (8.8) *relation between the entropy per particle and Q is not given by the simple expression* (2.10).

Up until this moment we kept parameters F and T in (8.8) independent. However, we are mostly interested in two particular cases: (i) $F = 1$ while

$T = T_{\mathrm{FD}}$ – arbitrary (distribution (2.4)); and (ii) $F < 1$ having arbitrary value, while T being fixed to T_ν – the temperature of neutrino background, related to the temperature of the cosmic microwave background today via $T_{\nu_0} = (4/11)^{1/3} T_{\mathrm{CMB},0}$ (distribution (2.20)).

We start with the case (i). Expressing ρ as a function of T_{FD}, we obtain

$$Q = \frac{g m^4}{\hbar^3} \mathbf{q} \, , \tag{8.13}$$

where numerical constant $\mathbf{q}$ is given by (c.f. [175]):

$$\mathbf{q} = \frac{\zeta^{5/2}(3)}{20\pi^2 \sqrt{15} \zeta^{3/2}(5)} \approx 1.96... \times 10^{-3} \, . \tag{8.14}$$

As a result for the distribution (2.4) and fixed number of particles, the quantity $\mathbf{Q}$ is independent on T_{FD}, volume or N. The entropy per particle is also independent on both T_{FD} and V and is given by

$$\frac{S}{N} = \mathbf{s} = I(1) \frac{2}{3\zeta(3)} \approx 4.20\ldots \tag{8.15}$$

Although both quantities S/N and $\mathbf{Q}$ are simply constants, we find it convenient to choose them in the form (2.10):

$$\frac{S}{N} = -\log\left(\frac{Q\hbar^3}{m^4}\right) + \log C_{\mathrm{FD}}, \quad C_{\mathrm{FD}} = g \cdot \mathbf{q} \cdot e^{\mathbf{s}} \approx g \times 0.1311\ldots \tag{8.16}$$

In case (ii) when $F \ll 1$ we obtain for S/N:

$$\frac{S}{N} = \frac{2}{3\zeta(3)} \frac{I(F)}{F} \simeq (1 - \log F) + \frac{2l}{3\zeta(3)} \, . \tag{8.17}$$

Similarly to (8.13)–(8.14)

$$\frac{Q\hbar^3}{m^4} = g \, \mathbf{q} \, F \, . \tag{8.18}$$

Combining (8.17)–(8.18) we can write

$$\frac{S}{N} = -\log\left(\frac{Q\hbar^3}{m^4}\right) + \log C_{\mathrm{NRP}}, \quad C_{\mathrm{NRP}} = g \, \mathbf{q} \exp\left(1 + \frac{2l}{3\zeta(3)}\right) \approx g \times 0.137\ldots \tag{8.19}$$

8.2.2 Mass bounds from the average phase-space density evolution

For illustration purposes we provide in Table 8.1 the average phase-space density estimator Q for all the dSphs, considered in this work, as well as

dSph	Q_f $\left[\frac{M_\odot}{\text{pc}^3}\left(\frac{\text{km}}{\text{sec}}\right)^{-3}\right]$	$m_{\text{FD,HD}}$ [keV]	$m_{\text{NRP,HD}}$ [keV]
Sextans	$5.68^{+10.67}_{-3.07}\cdot 10^{-6}$	$0.324^{+0.098}_{-0.057}$	$1.04^{+0.44}_{-0.24}$
Fornax	$8.86^{+12.77}_{-4.40}\cdot 10^{-6}$	$0.362^{+0.091}_{-0.051}$	$1.20^{+0.42}_{-0.25}$
Leo I	$1.55^{+3.08}_{-0.85}\cdot 10^{-5}$	$0.416^{+0.131}_{-0.075}$	$1.45^{+0.64}_{-0.34}$
UrsaMinor	$1.78^{+2.70}_{-0.90}\cdot 10^{-5}$	$0.431^{+0.112}_{-0.070}$	$1.52^{+0.55}_{-0.32}$
Bootes	$3.78^{+2.24}_{-1.48}\cdot 10^{-5}$	$0.520^{+0.064}_{-0.061}$	$1.95^{+0.33}_{-0.30}$
Draco	$3.21^{+1.27}_{-0.82}\cdot 10^{-5}$	$0.499^{+0.044}_{-0.036}$	$1.85^{+0.22}_{-0.17}$
Carina	$2.60^{+3.42}_{-1.25}\cdot 10^{-5}$	$0.474^{+0.111}_{-0.072}$	$1.72^{+0.56}_{-0.34}$
Sculptor	$5.93^{+4.30}_{-2.35}\cdot 10^{-5}$	$0.582^{+0.085}_{-0.069}$	$2.27^{+0.45}_{-0.35}$
Leo II	$6.39^{+6.60}_{-2.73}\cdot 10^{-5}$	$0.593^{+0.115}_{-0.077}$	$2.32^{+0.62}_{-0.40}$
Canes Venatici I	$6.16^{+4.11}_{-1.94}\cdot 10^{-6}$	$0.330^{+0.045}_{-0.030}$	$1.07^{+0.20}_{-0.13}$
Ursa Major I	$1.94^{+1.74}_{-0.84}\cdot 10^{-5}$	$0.440^{+0.077}_{-0.058}$	$1.56^{+0.37}_{-0.27}$
Hercules	$2.68^{+4.45}_{-1.53}\cdot 10^{-5}$	$0.477^{+0.132}_{-0.091}$	$1.74^{+0.67}_{-0.43}$
Leo T	$6.26^{+9.78}_{-3.16}\cdot 10^{-5}$	$0.590^{+0.157}_{-0.095}$	$2.31^{+0.85}_{-0.48}$
Ursa Major II[1]	$1.13^{+1.61}_{-0.55}\cdot 10^{-4}$	$0.685^{+0.169}_{-0.104}$	$2.81^{+0.96}_{-0.55}$
Leo IV	$3.35^{+40.91}_{-2.27}\cdot 10^{-4}$	$0.898^{+0.814}_{-0.221}$	$4.04^{+5.51}_{-1.27}$
Canes Venatici II	$5.91^{+10.61}_{-3.16}\cdot 10^{-4}$	$1.03^{+0.30}_{-0.18}$	$4.88^{+1.99}_{-1.10}$
Coma Berenices	$5.46^{+8.96}_{-2.61}\cdot 10^{-4}$	$1.01^{+0.28}_{-0.15}$	$4.75^{+1.82}_{-0.92}$

Table 8.1: The mass bounds, based on the evolution of the average phase-space density Q [175, 176]. The bound is provided for illustration purposes only (see Appendix 8.2.2 for discussion).

the lower mass bounds, based on the inequality (2.9) for Q during the evolution [175, 176] (for detailed discussion see Section 2.2). The value of Q_f, shown in the second column of the Table 8.1 is calculated from the data in the columns (3–4) of the Table 2.4, using formula (2.26) (with $\eta = 1$) and Q_i is defined via (2.8) for the momentum distributions (2.4) and (2.20) (for the bounds $m_{\text{FD,HD}}$ and $m_{\text{NRP,HD}}$ correspondingly). The results for Leo IV are quoted in (2.43) (Section 2.6).

8.3   Appendixes for Chapter 3

8.3.1   Selection criteria for dark matter distributions

We have collected from the literature 1095 dark matter profiles for 357 objects (from dwarf spheroidal galaxies to galaxy clusters, see Table 3.1 below). For each dark matter profile in our sample we have performed a number of checks. Those profiles have not passed these checks were rejected from subsequent analysis. As a result of the selection process we were left with 805 dark matter profiles for 289 objects.

– When analysing the data, we realized that for some objects the value of $r_\star$ lies well outside the region covered by the observational data, R_{data}. Such objects systematically show extremely high values of $r_\star$. For example, we found 37 galaxy profiles having $r_\star > 100$ kpc, while their kinematic data usually extends only up to $R_{\mathrm{data}} \sim 10 - 30$ kpc.

  Therefore, we select only dark matter profiles having $r_\star < 2.75 R_{\mathrm{data}}$. The coefficient 2.75 is justified by the following argument. The circular velocity in an NFW halo is given by

$$v_c^2(r) = \frac{G_N M_{\mathrm{NFW}}(< r)}{r} = 4\pi G_N \rho_s r_s^3 \frac{\log(1 + \frac{r}{r_s}) - \frac{r}{r+r_s}}{r}. \tag{8.20}$$

  For $r \ll r_s$ this function can be approximated as

$$v_c^2(r) \approx 2\pi G_N \rho_s r_s \left(r - \frac{4r^2}{3r_s} + \dots \right) \tag{8.21}$$

  In the part of the velocity curve where $\frac{4r^2}{3r_s}$ is much less than the errors on the velocity dispersion one cannot reliably determine r_s and ρ_s (since $v_c^2(r)$ is indistinguishable from a straight line, proportional to $\rho_s r_s$). It is important to have data points in the region where the contribution of the quadratic term becomes noticeable to reliably extract both NFW parameters. We chose to set $2.75 R_{\mathrm{data}} \geq r_\star$, which corresponds to a $\sim 50\%$ contribution from the second (quadratic) term to $v_c^2(r)$. Similar criteria are used for ISO and BURK profiles. This reduces the number of considered profiles from 1095 to 891.

– For 76 objects both NFW and ISO (or BURK) dark matter profiles were available. For these objects we checked the relation between the parameters of these profiles against the results shown in Eq. (3.16) (or Eq. (3.18)

for BURK). Results of this comparison for the NFW and ISO profiles are shown in Fig. 3.4. This figure shows that there is indeed a maximum in the region defined by Eq. (3.16) but also that the scatter around this maximum is pretty large and that the difference between measured and expected ratios of NFW and ISO parameters can be as large as a factor of ten. Therefore we decided to exclude from our sample all objects with a ratio ρ_s/ρ_c, r_s/r_c, (or ρ_s/ρ_B, r_s/r_B for BURK profiles) larger than a factor 5 with respect to the theoretical prediction shown in Eq. (3.16) or (3.18).

– Finally, in several cases parameters of dark matter density profiles were quoted with very large uncertainties. We decided to select only those profiles for which the ratio between the 1σ upper and lower bounds of quoted parameters (radius $r_\star$ or the density $\rho_\star$) was smaller than a factor of 10.

To compare the $\mathcal{S} - M_{\text{halo}}$ relation for selected objects with N-body simulations, we used the results from [307]. This suit of ΛCDM numerical simulations probed the halo mass range $10^{10} - 10^{15} M_\odot$. For each simulated halo of [307] we computed M_{halo}, fit the particle distribution to the NFW density profile and calculate $\mathcal{S}$ using Eqs.(3.9) and the definition (3.7). The observational data together with results from simulations is plotted of the Fig. 8.1. The small scatter of the simulation points at $M_{\text{halo}} \gtrsim 10^{14} M_\odot$ is explained by the finite size of the simulation box. The simulations with the large box size (e.g. [310]) verify that the scatter does not reduce at large masses (c.f. the pink shaded region on the Figure 1).

8.3.2 Summary of collected dark matter distributions

We collected from the literature 1095 dark matter density profiles for 357 unique objects ranging from dSphs to galaxy clusters. For each dark matter profile found in our sample we have applied uniform selection criteria:

– If for an object several independently determined profiles were available and all of them but one agreed in the values of $r_\star$ and $\rho_\star$ within a factor of 5, we rejected the outlier.

– For some objects the best-fit value of the characteristic radius $r_\star$ was extrapolated well outside the region covered by the observational data, R_{data}. In this case the parameters of the density profile had extremely large uncertainties. We have thus rejected objects with $r_\star < 2.75 R_{\text{data}}$.
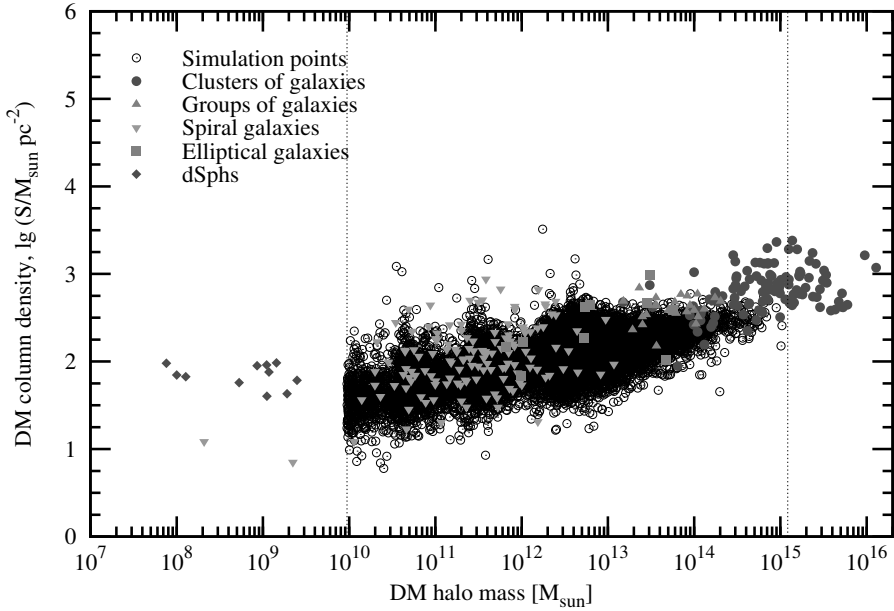
Figure 8.1: **Dark matter column density as a function of the halo mass.** Similar to the Figure 1, we plot 289 objects, selected in Section 8.3.1 above (coloured shapes) superimposed on the simulation data for isolated halos [307] (open black circles).

– We rejected profiles for which the uncertainty in any quoted parameter ($r_\star$ or $\rho_\star$) was higher than a factor of 10.

– For objects with more than one profile selected, the average value of $\mathcal{S}$ and M_{halo} was used in the subsequent analysis.

– When processing the data of N-body simulations we used the fit of particle distribution by the NFW density profile and computed $\mathcal{S}$, using equation (3.7).

– If *the same* observational data is fit by several different dark matter profiles (e.g. NFW, ISO, and BURK), one can then find a relation between characteristic scales $r_\star$ and densities $\rho_\star$ of these profiles. Provided such a relation holds, the difference between the column densities $\mathcal{S}_{\mathrm{NFW}}$, $\mathcal{S}_{\mathrm{BURK}}$ and $\mathcal{S}_{\mathrm{ISO}}$ turns out to be less than 10%. Qualitatively, this can be un-

derstood as follows: to explain the same velocity data, two dark matter profiles should have roughly the same mass within some radius R_0. If both profiles happen to have the same behaviour at large distances, their $\mathcal{S}$ values, averaged over R_0 will be essentially equal. This explains the use of $\mathcal{S}$ as a characteristic of dark matter halos.

8.4 Appendixes for Chapter 5

8.4.1 Cleaning of soft proton flares

EPIC external "flaring" background is caused by protons of energies less than a few $\times 100\,\mathrm{keV}$, collected by the X-ray mirrors. These protons originate in the Earth's magnetosphere. During the flaring periods, the background level increases by one-two orders of magnitude. According to [329] they have very hard and unpredictable spectral shape usually dominating at high energies which makes their modeling technically challenging. In addition to that, due to their different convolution with effective area comparing to X-ray photons they are responsible for some artificial line-like features, for instance at $\sim$2.5 keV [323].

Several different procedures have been developed by different authors. For completeness we present their brief overview here.

1. The "standard" method used by [334] is based on the construction of ≥ 10 keV lightcurves for single pixel events binned by 100 s. The intervals having more 0.2 cts/s for MOS1/MOS2 and 0.45 cts/s for PN cameras in this energy range are rejected. However, the authors find that some flares "survive" after this procedure creating the variability in 1-10 keV band. This effect is attributed to the existence of lower energy protons at the edges of the encountered proton "clouds". Therefore, the additional screening at 1-10 keV range (allowing MOS countrates to be smaller than 1.15 cts/s) is performed.

2. In [330], the authors developed an algorithm to obtain an automated and homogeneous screening from the flaring non-X-ray background. During the first step, the 0.4-12 keV MOS lightcurves were extracted from events coming to the instrument's FoV and binned by 30 s intervals. Then, the histogram of count rates is created. After fitting this histogram with a Gaussian function, the intervals having the countrate

more than 3.3 σ larger than the mean value are rejected. After the rejection, additional test of the high-energy countrates is performed by using the events from parts of MOS CCDs located *not* in the instrument's FoV. Because at high energies ($\gtrsim 5\,\mathrm{keV}$) the blank-sky spectrum is dominated by the instrumental background [326, 334], comparison of in-FoV and out-FoV countrates at these energies may idenfity the additional in-FoV high-energy component caused by soft proton flares passed through their 3.3 σ filter.

3. In [326], the authors used the "double filtering" procedure removing time intervals with either high-energy (9.5-12 keV for MOS, 10-14 keV for PN) and low-energy (1-5 keV) countrates deviating more than by 20 % for the average values. Such a filtering removed ~ 35 % of MOS and ~ 45 % of PN uncleaned exposure.

4. In [353], the authors first apply the lightcurve filtering in a wide band (0.2-12 keV for MOS) camera. After removing time intervals with countrate above 2-2.5σ above the mean level, they perform the point source detection procedure. After removal the point sources, they again perform the lightcurve cleaning. Due to removal of point sources, the sensitivity for for faint flare search is significantly increased allowing them to exclude additional $\sim$10 % of exposure affected by the smallest flares.

5. In [329], the authors idenfitied the flaring intervals using the procedure similar to [330]. By cleaning time intervals with 2.5-8.0 keV MOS countrates exceeding more than by 2.5 σ the mean value, they remove ~ 36 % of MOS uncleaned exposure. In addition, the authors model the remaining soft proton component with the broken powerlaw (without convolving with the instrument effective area) with $E_{br} \simeq 3.2$ keV.

6. In [328], the authors first exclude time bins where the high-energy (10-12 keV) MOS countrate is larger than 0.2 cts/s (for 100 s bins). After that, a 2-5 keV histogram is produced and modeled similar to [330] and all bins with countrates more than 3σ above the mean value are also rejected. Finally, $F_{in} - F_{out}$ diagnostic of [330] is used to estimate the residual soft proton flare contamination. All observations with $F_{in} - F_{out}$ less than 1.5 were used for subsequent analysis.

7. In [421, 422], the authors use the procedure `mos-filter`, developed

by the authors of [329] as a part of *XMM-Newton* Extended Sources Analysis Software (XMM-ESAS), now the part of XMM SAS. In this procedure, 2.5-12 keV lightcurve is binned by 1 s intervals and all intervals with count rates different from mean value more than by 1.5 σ were rejected.

8.4.2 Modeling closed-filter spectra.

In this Section, we model closed-filter spectrum in Xspec using very simple powerlaw model in 2.3-10.0 keV energy range. The energy bins around strong instrumental lines (namely, 5.3-5.7, 5.8-6.0, 6.3-6.6, 7.4-7.7, 8.0-8.2, 8.5-8.8, 9.5-9.8 keV for MOS cameras and 5.3-5.7, 5.8-6.0, 6.3-6.6, 7.0-9.1, 9.3-9.7 keV) are removed. The results of fit are very good, see Table 8.2 and Fig. 8.2 for details. The measurements of the powerlaw index are consistent with previous results of [334] (who obtained $\alpha_{hard} \sim 0.2$, $\alpha_{soft} \sim 0.8$ and $E_{br} \sim 1$ keV for MOS cameras) and [326] (who obtained $\alpha_{soft} = 0.7 - 0.8$, $E_{br} = 1.3 - 1.5$ keV and $\alpha_{hard} = 0.4$ for PN and $\alpha_{hard} = 0.1 - 0.2$ for MOS cameras). The large difference between the values α_{hard} between MOS and PN cameras is *not* unexpected. According to [334], about ~ 99 % of cosmic rays are rejected by internal electronics by using multiple pixel analysis (due to large energy deposition of cosmic rays they mostly interact with several adjacent CCD pixels). The sizes of CCD pixels for MOS (1.1 arcsec) and PN (4.1 arcsec) are very different, so we expect the very different outcome of internal rejection of cosmic rays in these cameras.

	MOS1	MOS2	PN
Fit quality, total χ^2/d.o.f.	360.5/369	373.6/369	831.0/849
Powerlaw index	0.183±0.007	0.177±0.007	0.402±0.010
Norm., cts/s/keV at 1 keV	0.0480±0.0006	0.0464±0.0006	0.090±0.002

Table 8.2: Model parameters of closed filter background on powerlaw continuum (without RMF or ARF).

8.4.3 Adding simulated lines to the combined dataset

Line simulations are performed using standard routine fakeit, a part of Xspec spectral fitting package [409]. We adopt the following procedure of
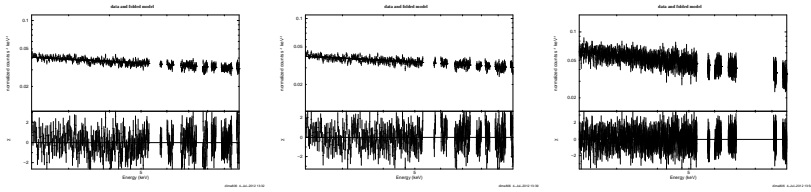
Figure 8.2: Best-fit continuum model and fit residuals for closed-filter background spectra from MOS1 (*left*), MOS2 (*centre*) and PN (*right*) cameras. The energy ranges containing strong instrumental lines are excluded from the fit, see text for details. The resulting energy bins are well modeled with simple `powerlaw` continuum, see 8.2 for details. This result ensures that we may really use *modeling* of closed-filter background, instead of *subtracting* it.

line simulation. First, we simulated a narrow line for each observation having the same flux (in photons cm^{-2}s^{-1}). The initial line energy and dispersion (set to 1 eV)[2] are kept the same. We repeat many times, adding the line to each individual observation, prior to stacking them together. In each energy bin (15 eV for MOS camera and 5 eV for PN camera) the total number of counts is allowed to vary according to Poisson distribution allowing to create different realizations of the line. The actual shapes of line broadening and effective area is taken into account by using instrument responses for each observation contained in RMF and ARF files, see Sec. 5.2.4 for details. After simulating spectra for each observation of our combined dataset, the spectra from each camera (MOS1, MOS2, PN) are dumped to text format using FTOOL `fdump`, binned by 60 eV per bin.

---

[2]Predicted internal dispersion of dark matter decay line due to Doppler broadening is about 10^{-3} times line energy for galaxies [229]. However, because total dispersion is the root of the squared sum of initial dispersion ($\lesssim 10$ eV) and line broadening ($\gtrsim 50$ eV), the corresponding error on total dispersion does not exceed 2% and is neglected henceforth.